

Stratified Spectral Mixture Analysis of Medium Resolution Imagery for Impervious Surface Mapping

Genyun Sun¹, Xiaolin Chen², Jinchang Ren³, Aizhu Zhang¹, Xiuping Jia²

¹School of Geosciences, China University of Petroleum (East China), Qingdao, Shandong 266580, China

²School of Electrical Engineering, The University of New South Wales at Canberra, ACT 2600, Australia

³Department of Electronic and Electrical Engineering, University of Strathclyde, Glasgow G11XQ, U.K.

Abstract

Linear spectral mixture analysis (LSMA) is widely employed in impervious surface estimation, especially for estimating impervious surface abundance in medium spatial resolution images. However, it suffers from a difficulty in endmember selection due to within-class spectral variability and the variation in the number and the type of endmember classes contained from pixel to pixel, which may lead to over or under estimation of impervious surface. Stratification is considered as a promising process to address the problem. This paper presents a stratified spectral mixture analysis in spectral domain (Sp_SSMA) for impervious surface mapping. It categorizes the entire data into three groups based on the Combinational Build-up Index (CBI), the intensity component in the color space and the Normalized Difference Vegetation Index (NDVI) values. A suitable endmember model is developed for each group to accommodate the spectral variation from group to group. The unmixing into the associated subset (or full set) of endmembers in each group can make the unmixing adaptive to the types of endmember classes that each pixel actually contains. Results indicate that the Sp_SSMA method achieves a better performance than full-set-endmember SMA and prior-knowledge-based spectral mixture analysis (PKSMA) in terms of R, RMSE and SE.

Key words—Impervious surface, Stratification, Spectral mixture analysis, CBI

1. Introduction

Impervious surface is defined as any area consisting of constructed surface which water cannot infiltrate to reach the soil (Yang et al, 2010; Weng, 2012), such as roads, roofs, and parking lots. It not only serves as a key indicator of the degree of urbanization, but also affects in the micro-ecosystem change (Wang et al, 2015). The increasing replacement of nature landscape by impervious surface leads to the change of hydrological character (White & Greer, 2006; Xian et al, 2007; Du et al., 2015), the generation of heat island effects (Kato & Yamaguchi, 2007; Yuan & Bauer, 2007; Coseo & Larsen, 2014), deterioration in water quality (Conway, 2007) and other

36 detrimental effects. Therefore, it is essential to monitoring impervious surface
37 distribution timely and accurately to ensure urban development is sustainable (Wu &
38 Murray, 2005; Du & Du, 2014).

39 Remote sensing technology has become an important method, and may be the
40 only viable way, to effectively extract impervious surface due to its high efficiency
41 and low cost with large coverage (Yang et al, 2010; Lu & Weng, 2006). Various
42 studies have been conducted for impervious surface mapping, with images from a
43 large range of satellite sensors and a variety of data sources, including MODIS images
44 with coarse spatial resolution (Yang & Lunetta, 2011; Deng & Wu, 2013), Landsat
45 TM/ETM+ and ASTER imagery (Hu & Weng, 2009; Sexton et al, 2013) with
46 moderate spatial resolution, and IKONOS and QuickBird data (Lu & Weng, 2009;
47 Zhou & Wang, 2008) with high spatial resolution. In addition to the optical remote
48 sensing data, some other types' data, such as nighttime photography (Kotarba &
49 Aleksandrowicz, 2016), Synthetic Aperture Radar (SAR) imagery (Zhang et al, 2016;
50 Zhang et al, 2014) and open social data (Hu et al, 2016), have also been studied on
51 their application to impervious surface estimation in recent years. Among them,
52 medium spatial resolution images might be a better choice for the urban impervious
53 surface mapping, because they provide a good trade-off among coverage, price, and
54 quality.

55 However, due to the heterogeneity of urban land covers and the limitation in
56 spatial resolution, the presence of mixed pixels has been recognized as a major
57 problem in the analysis of medium spatial resolution images (Weng, 2012). Several
58 unmixing methods have then been applied for impervious surface extraction,
59 including linear spectral mixture analysis (LSMA) (Weng et al, 2009; Hu & Weng,
60 2008; Yang & He, 2017), artificial neural network (ANN) (Mohapatra and Wu, 2008),
61 regression analysis (Yang et al, 2003; Yang & Liu, 2005; Kaspersen et al., 2015) and
62 regression trees (Huang & Townshend, 2003; Deng & Wu, 2013). Yet LSMA is still
63 the most popular approach due to its simplicity and physically-based description of
64 the fractions of different land covers (Small & Milesi, 2013; Burazerovic et al, 2013).

65 While LSMA and LSMA based methods are easy to use in estimating impervious
66 surface, several problems still exist. It has been found that impervious surface tends to
67 be overestimated in the areas with small amounts of impervious surface, but is
68 underestimated in the areas with large amounts of impervious surface (Weng, 2012;
69 Lu and Weng, 2006). The similarity in spectral properties between impervious and
70 pervious surface, especially impervious surface and soil, can be one of the main
71 reasons for underestimation in urban area and overestimation in pervious area.
72 Another problem is the difficulty in selecting endmembers due to within-class spectral
73 variability (Foody et al, 1997). It should be noted that the differences in type,
74 geometry and illumination etc. lead to the huge differences in term of spectral
75 characteristics of impervious surface. Therefore, using one endmember to represent
76 all types of impervious surfaces is often found problematic (Weng et al, 2008). The
77 performance of LSMA can also be reduced if every pixel in the image is unmixed into
78 a fix set of endmembers, where some pixels may only contain a subset of
79 endmembers.

80 Stratification is considered as a promising process to solve these problems. In
81 (Lu & Weng, 2004), stratification of a whole scene into subareas with similar
82 landscape structures is suggested to improve impervious surface mapping. Several
83 studies (Wu & Murray, 2003; Zhang et al, 2014; Small, 2001; Somers et al,2009) have
84 attempted to employ different endmember class sets for urban and rural areas.
85 However, the endmembers sets applied to each subarea are extracted from the entire
86 image scene. The weakness of this treatment is the spectral variability in different
87 subsets is not considered. The endmembers, which are selected at the extreme of an
88 n-dimensional scatter plot of the entire image may be less representative as the pure
89 pixels in each subset (Deng & Wu, 2013). The current methods stratify a remote
90 sensed image into urban and rural areas through spatial information, such as texture
91 and road density information (Zhang et al, 2014; Liu & Yang, 2013). The overlooked
92 the spectral information would result in mis-estimation of land cover abundances.

93 In this study, we address the above mentioned problems and propose a stratified
94 spectral mixture analysis in spectral domain (Sp_SSMA) for impervious surface
95 mapping. We clipped an image data set into three groups to reduce the within class
96 variability in each subgroup based on three spectral character components, namely
97 Combinational Build-up Index (CBI)(Sun et al, 2015), Normalized Difference
98 Vegetation Index (NDVI) (Rouse et al, 1974) and color intensity. Then, endmembers
99 are selected from each group independently rather than from the entire image to cope
100 with the within class variability. An endmember set with different types and numbers
101 is applied in each group to make it more adaptive. Impervious surface fractions are
102 estimated by LSMA and the results of the three subgroups are combined to produce a
103 complete map.

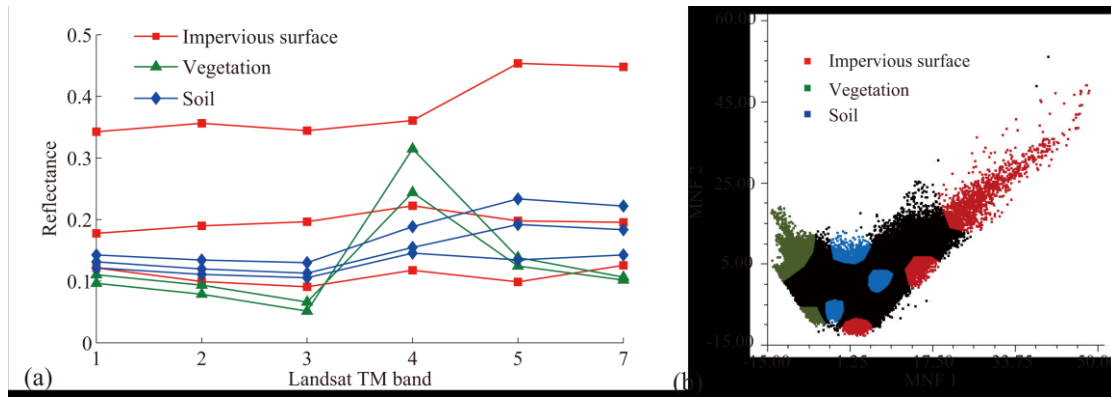
104 The remainder of this article is structured as follows. The second section presents
105 the methodology of Sp_SSMA, including the stratification, the selection of
106 endmembers and the procedures for deriving impervious surface abundance. The third
107 section introduces the study areas and remotely sensed data, including data
108 preprocessing. The comparative results and discussions are reported in Section 4.
109 Finally, conclusions are provided in Section 5.

110 2. Methodology

111 Based on the definition, impervious surface is a unifying theme. However it
112 consists of a number of artificial features which have different spectral profiles in
113 general. Figure 1(a) illustrates the mean spectral values of different impervious
114 surface and other major land cover classes based on the pure pixels selected from a
115 Landsat TM image. It indicates that not only impervious surfaces consist of different
116 structures, colors, and materials, vegetation and soil also show great spectral
117 differences within each of them. Figure 1(b) is the corresponding grouped scatter
118 points of the sampled pixels in the feature space composed by the first two
119 components of minimum noise fraction (MNF1 and MNF2). We can see that the pure
120 pixels are not always located at the extremes of the scatter plot as it supposed to be
121 theoretically, due to the within-class variation of a land cover type. It also indicates

122 the spectral variability within several classes as well as the spectral confusion among
123 several land covers, especially between urban impervious surfaces and bare soil.

124 Therefore, simply extracting a single set of endmembers from the vertices in an
125 n-dimensional scatter plot of an entire scene, like the treatment in (Powell, et al, 2007),
126 is potentially less reliable because they cannot account for the considerable
127 within-class variability (Rashed et al, 2003; Roessner et al, 2001). The similarity of
128 spectral characteristics between impervious and pervious surface, especially bare soil,
129 also prevent the SMA-based methods from achieving a promising result.

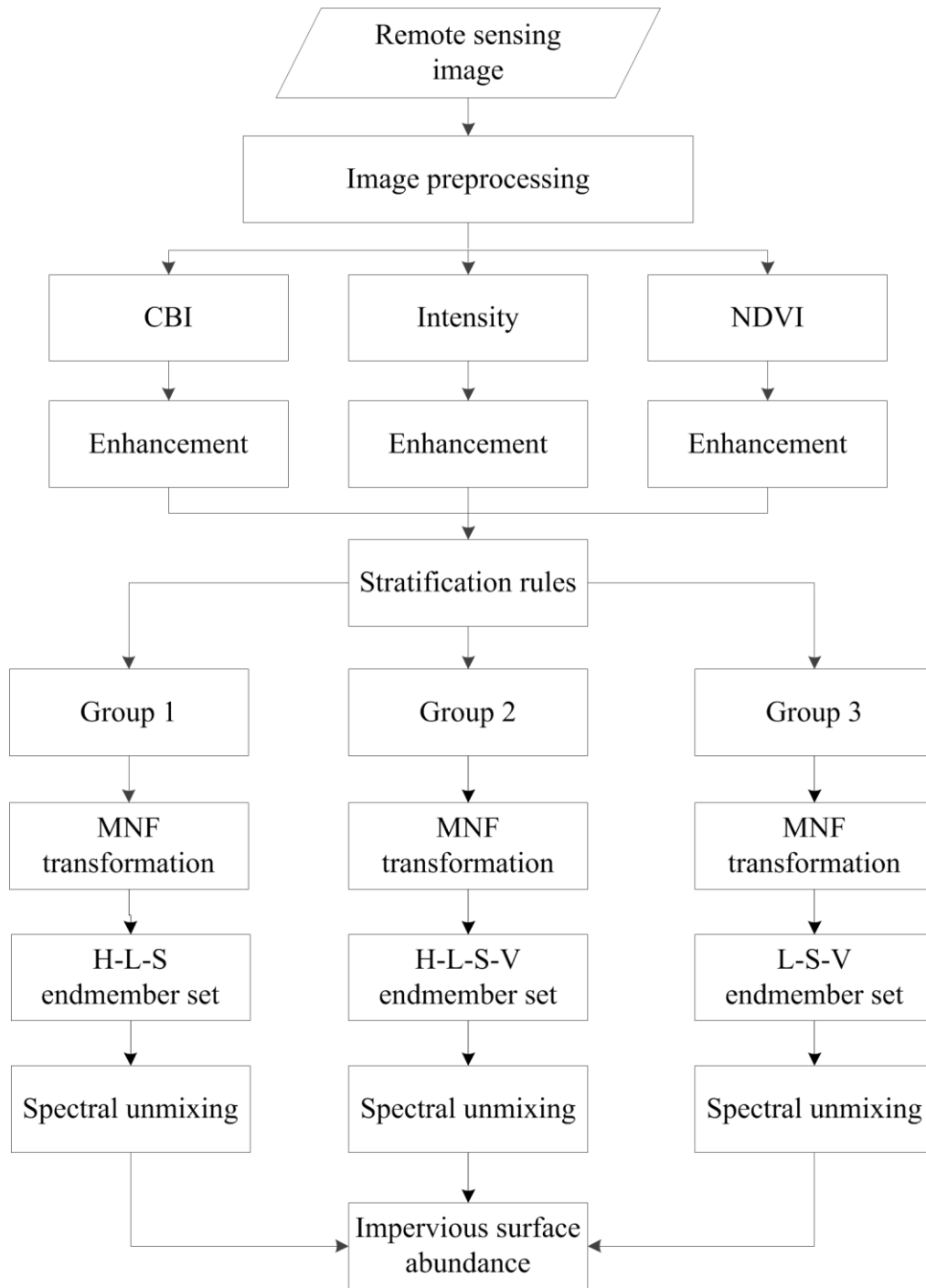


130

131 Figure 1 Reflectance of land feature endmembers (a) and the corresponding feature space representation of the first
132 two MNF components for Landsat TM reflectance image (b).

133

134 To tackle this problem, we develop a stratified spectral unmixing method in
135 spectral domain (Sp_SSMA). Three spectral feature components, CBI, intensity
136 component of intensity-hue-saturation (IHS) and NDVI, are utilized to partition the
137 entire data into three groups, named Group 1, Group 2 and Group 3. Each group is
138 processed independently, including endmember extraction and spectral unmixing, to
139 minimize the within class spectral variability and the confusion between some urban
140 features and non-impervious land covers. The major steps in Sp_SSMA are described
141 in Figure 2.



142

143 Figure 2 Flowchart of the Sp_SSMA method.

144

145 *2.1 Stratification*

146 *2.1.1 CBI calculation*

147 CBI is a feature-extraction based spectral impervious surface index. It reduces

148 the original multi-/hyper-bands into three thematic-oriented features. They are the first
 149 component of a principal component analysis (PC1), Normalized Difference Water
 150 Index (NDWI) (Gao, 1996) and Soil Adjusted Vegetation Index (SAVI) (Huete, 1988),
 151 to represent high albedo, low albedo and vegetation respectively. The features are
 152 calculated using the following equations (Sun et al, 2015):

$$153 \quad CBI = \frac{(PCI_{nor} + NDWI_{nor})/2 - SAVI_{nor}}{(PCI_{nor} + NDWI_{nor})/2 + SAVI_{nor}} \quad (1)$$

154 with

$$155 \quad SAVI = \frac{(\rho_{NIR} - \rho_{RED})(1+L)}{\rho_{NIR} - \rho_{RED} + L} \quad (2)$$

$$156 \quad NDWI = \frac{\rho_{GREEN} - \rho_{NIR}}{\rho_{GREEN} + \rho_{NIR}} \quad (3)$$

157 where ρ_{GREEN} , ρ_{RED} , ρ_{NIR} represent the reflectance value of GREEN, NIR and
 158 SWIR bands, respectively. L is a correction factor ranging from 0 to 1. In this study,
 159 0.5 is taken to form a vegetation image. PCI_{nor} , $SAVI_{nor}$ and $NDWI_{nor}$ are the
 160 normalized PC1, SAVI and NDWI respectively.

161 In CBI, impervious surfaces are highlighted with positive values, vegetation is
 162 represented with negative values while bare soil and mixed land cover types are
 163 associated with numerical values about zero. Qualitative and quantitative assessments
 164 of accuracy analysis, separability between impervious surface and soil at different
 165 spatial and spectral resolutions as well as comparison with other indices indicate that
 166 CBI is a promising and reliable urban landscape index for mapping impervious
 167 surface areas (Sun et al, 2015).

168 2.1.2 I calculation

169 The IHS color space can be regarded as a two-dimensional color vector and one
 170 intensity vector (Córdoba-Matson et al, 2010). That is to say, the spectral magnitude
 171 of a land feature mainly lies in the intensity component, which is expressed as

$$172 \quad I = \sum_{i=1}^n \rho_{VIR-i} / n \quad (4)$$

173 where ρ_{VIR-i} is the i th VIR band of a pixel, n is the total number of VIR bands. The
 174 intensity value of the bright impervious surface tends to show the largest distinction
 175 with the background land features.

176 2.1.3 NDVI calculation

177 NDVI (Rouse et al, 1974) is an effective index to measure vegetation content
 178 which employs the peak and valley reflectances at NIR and RED bands to form the
 179 vegetation index (Huete, 1988). In this study, NDVI is utilized to make the distinction
 180 of vegetation due to their high NDVI values. The NDVI is calculated using Eq. (5)

181 (Rouse et al, 1974).

$$182 \quad NDVI = \frac{\rho_{NIR} - \rho_{RED}}{\rho_{NIR} + \rho_{RED}} \quad (5)$$

183 where ρ_{RED} and ρ_{NIR} represent the reflectance values of GREEN, NIR and SWIR
184 bands, respectively.

185 2.1.4 Threshold selection

186 The threshold selection for stratification is crucial to delineate the biophysical
187 distribution of the impervious surface from other land covers. In this study, a
188 transformation (Liu et al, 2011) was utilized to improve the separability between
189 different land cover types. The gray-scaled index images, namely CBI, I and NDVI,
190 were enhanced by adopting Eq. (6) (Liu et al, 2011).

$$191 \quad i_{enh} = \left(\frac{1}{\pi} \arctan[\lambda\pi(i_{nor} - \theta)] + 0.5 \right) \sqrt{i_{nor}} \quad (6)$$

192 Where i_{enh} is the enhanced index map, i_{nor} is the normalized index map, λ is a
193 sensitivity factor and θ is the coarse estimation of mean value of the target land
194 cover type, or more precisely impervious surface in CBI and I while vegetation in
195 NDVI.

196 The enhanced intensity maps are used to stratify the whole image. Otsu (Otsu,
197 1979) proposed a histogram-based threshold selection method that is suitable for
198 separating an object from its background. We use this method to automatically select
199 the threshold T for stratification. In Otsu's method (Otsu, 1979), a threshold T is
200 selected to maximize

$$201 \quad \sigma^2(T) = \frac{(\mu\omega_1(T) - \omega_2(T))^2}{\omega_1(T)\omega_2(T)} \quad (7)$$

202 where $\omega_1(T) = \sum_{i=0}^T p_i$, $\omega_2(T) = \sum_{i=T+1}^{255} p_i$, $\mu = \sum_{i=0}^{255} ip_i$, and p_i is the probability of
203 the gray level i. T_{CBI} , T_I and T_{NDVI} , the threshold of the enhanced CBI, I and NDVI
204 respectively, are obtained using Eq. (7) and used to stratify the image. Three groups
205 are defined as follows.

206 Group 1: $CBI_{enh} > T_{CBI}$, $I_{enh} > T_I$ and $NDVI_{enh} < T_{NDVI}$

207 Group 3: $CBI_{enh} < T_{CBI}$ and $NDVI_{enh} > T_{NDVI}$

208 Group 2: $((CBI_{enh} < T_{CBI}) \cap (NDVI_{enh} < T_{NDVI})) \cup ((CBI_{enh} > T_{CBI}) \cap$
209 $(I_{enh} < T_I)) \cup ((CBI_{enh} > T_{CBI}) \cap (I_{enh} > T_I) \cap (NDVI_{enh} > T_{NDVI}))$, (i.e. is the
210 remaining region.)

211 2.2 Endmember selection

212 Endmember extraction is critical. In this study, endmembers were selected in

213 each group independently, rather than from the entire image, to achieve more adaptive
 214 spectral characters. The endmember selection in each subset follows the usual
 215 minimum noise fraction (MNF)-based procedure. Spectral feature spaces were
 216 generated using the first three MNF components, and the typical pure pixels are those
 217 located at the extreme vertices of the data cloud in the scatter plots. Endmembers of
 218 the three sub-regions were indentified from the vertices of the scatterplots in each
 219 sub-scene independently. The extreme or less extreme pure pixels in the original
 220 image located at the extreme points in different groups so as to balance the within
 221 class variation and easy implement of extreme pixels selection. The number and type
 222 of endmember sets in each sub-region is determined based on the corresponding
 223 respective biophysical characteristics.

224 The combined criteria of Group 1 can make it reasonable to treat Group 1 data as
 225 containing no vegetation component. That is to say, Group 1 is composed of
 226 impervious surface and soil with vegetation pixels masked out by intensity component
 227 and NDVI. In contrast, the area of Group 3, which contains a low CBI value and high
 228 NDVI value, is mainly composed of vegetation and soil, with small amount of low
 229 albedo impervious surface. As for Group 2, impervious surface (high albedo and low
 230 albedo), soil and vegetation form the land cover features. Therefore, different
 231 endmembers are defined for each Group as follows.

232 Group 1: high-albedo, low albedo and soil (H-L-S).

233 Group 2: high albedo, low albedo, soil and vegetation (H-L-S-V).

234 Group 3: low-albedo, soil and vegetation (L-S-V).

235 2.3 Impervious surface estimation

236 The LSMA approach is physically based on the assumption that the spectrum for
 237 each pixel is a linear combination of all endmembers in the pixel (Wu, 2004) with the
 238 proportions of the endmembers representing the percentage of the land feature. The
 239 fraction image of each endmember is estimated through inversion of the linear
 240 combination with the spectral proportions of the endmembers representing the
 241 percentage of the land feature. LSMA was also under the assumption that no
 242 interaction between the photons reflected by each component. [With these assumptions,](#)
 243 [a LSMA with full abundance constraints can be expressed as \(Lu & Weng, 2006\):](#)

$$244 \quad R_b = \sum_{i=1}^N f_i R_{i,b} + e_b \quad (8)$$

245 where

$$246 \quad \sum_{i=1}^N f_i = 1 \wedge f_i \geq 0 \quad (9)$$

247 where R_b is a mixed pixel's reflectance at band b, N is the number of endmembers,

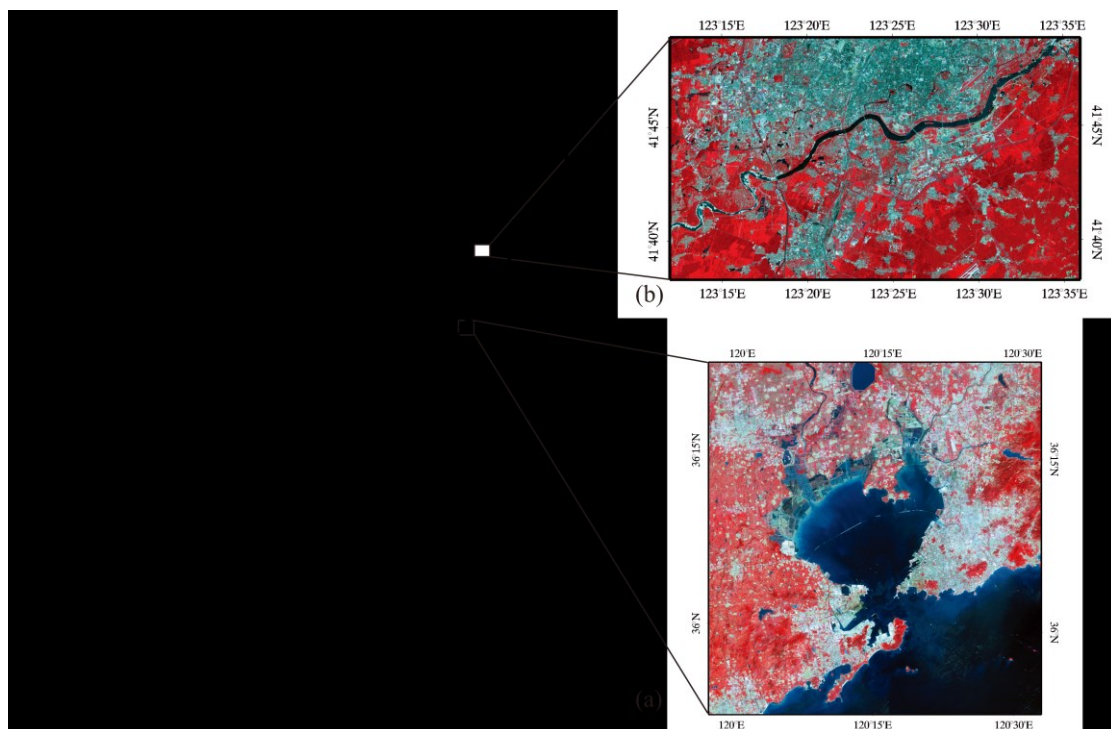
248 $R_{i,b}$ is the reflectance of endmember i at band b, f_i is the fraction of endmember i,

249 and e_b is the residual error.

250 As high and low albedo endmembers both are associated to impervious surface,
251 the final impervious surface fraction is calculated by summing the abundance of high
252 and low albedo endmembers for each mixed pixel. Then, the impervious surface
253 abundance in the three urban subsets was mosaicked to build the final regional
254 impervious surface abundance map.

255 3 Study area and data

256 Multi-sensor data, namely Landsat TM and ASTER, with two study sites were
257 investigated to test the proposed Sp_SSMA algorithm (Figure 3).



258 Figure 3 The location of study area: (a)The false color image covering the Qingdao city, China, illustrated with
259 Landsat TM image (R: band 4, G: band 3, B: band 2), (b)The false color image covering the Shenyang city, China,
260 illustrated with ASTER image (R: band 3, G: band 2, B: band 1).
261

262 3.1 Landsat TM imagery

263 The first study area is an urban transect in the region of Qingdao, China. As
264 shown in Figure 3(a), a scene of Landsat TM image acquired on July 15, 2009 was
265 employed for this study, suggesting that a large diversity of land cover properties
266 present within the study area. Different impervious surfaces, such as residential areas,
267 mixed-use areas, commercial and industrial districts, are shown in the image.
268 Non-urban land cover types include water bodies, green vegetation and bare soils.

269

270 The city of Qingdao is situated in the south of the Shandong Province, adjacent
271 to the Huanghai Sea (Figure 3(a)). As an important region in Eastern China, Qingdao
272 has seen rapid development. The annual GDP reached 869.2 billion Yuan in 2014,
273 with an increase of 8.0%, ranking first in Shandong Province and fourteenth out of
274 China's top 20 cities. The fast economic growth is accompanied by rapid urbanization,
275 causing transformation from nature environment to man-made surface. As for urban
276 area, the historic town is located in the eastern part of the study area while the new
277 district mainly lies in the western part. The suburban area is dominated by forest land
278 while agriculture land located mainly in the northern part of the study area.

279 3.2 ASTER imagery

280 The second study area (Figure 3(b)), located in Shenyang, China, is a typical
281 heavy industrial area since early 1900s. Aster imagery was collected over the area on
282 August 17, 2004. Shenyang is the provincial capital and largest city of Liaoning
283 Province, as well as an important heavy industrial base and a transportation hub in
284 Northeast China. Under the reform and open policies, Shenyang has experienced
285 sustained and high speed growth and urbanization since the late 1970s. After the
286 “revitalizing the old industrial bases in Northeastern China” strategy in 2003,
287 Shenyang was identified as the core of the new-industrialization zone for national
288 demonstration (Zhang et al, 2007). It is expected to offer a demonstration for China’s
289 change in industrial and economic development mode. Under such circumstances,
290 Shenyang’s urbanization will definitely continue to increase rapidly, and a more
291 complex landscape resulting from industrial transformation will be observed.

292 3.3 Data preprocessing

293 The Landsat TM image has six spectral bands (except the thermal band) with a
294 spatial resolution of 30m. The ASTER image has 9 bands with different spatial
295 resolutions (except the thermal bands), two visible bands, and one near infrared (NIR)
296 band with the spatial resolution of 15 m, six short wavelength IR (SWIR) bands with
297 30m resolution. The 15m ASTER bands were resampled to 30m with the application
298 of nearest-neighbor resampling algorithm.

299 Atmospheric correction was applied to neither of the images due to generally
300 good weather condition. Radiation calibration was conducted prior to data processing.
301 With the Landsat TM and ASTER reflectance images, water pixels were identified
302 and removed with the help of unsupervised classification. Additionally, the Google
303 Earth images acquired on July 22, 2009 and Oct 19, 2004 were used as ground
304 reference data for accuracy assessment respectively.

305

306 4 Experimental Results and Discussions

307 4.1 Experimental design

308 To evaluate the performance of the proposed method for mapping impervious
309 surface abundance and distribution, the corresponding Google Earth images, which
310 were generated near the acquisition date of Landsat TM and ASTER images
311 respectively, were used as the ground reference. The spatial resolution of Google
312 Earth images in both study areas is 0.5 m and each pixel is then treated as pure pixel.

313 After obtaining the estimation for the actual imperviousness and estimated
314 imperviousness, three quantitative estimators were adopted to assess the accuracy of
315 impervious surface abundance modeled by Sp_SSMA. They are correlation
316 coefficient (R), root mean square error (RMSE) and systematic error (SE).
317 Specifically, R means the statistical relationships between the estimated and actual
318 imperviousness, RMSE reflects the relative estimated errors of impervious surface
319 abundances, and SE measures the bias, an overall tendency of over- or
320 under-estimation. These three accuracy metrics can be calculated using Eqs. (11) to
321 (13) respectively as follows.

$$322 R = \frac{\sum_{i=1}^N (f_i - \bar{f})(\hat{f}_i - \bar{\hat{f}})}{\sqrt{\sum_{i=1}^N (f_i - \bar{f})^2 \cdot \sum_{i=1}^N (\hat{f}_i - \bar{\hat{f}})^2}} \quad (11)$$

$$323 RMSE = \sqrt{\frac{1}{N} \sum_{i=1}^N (\hat{f}_i - f_i)^2} \quad (12)$$

$$324 SE = \frac{1}{N} \sum_{i=1}^N (\hat{f}_i - f_i) \quad (13)$$

325 where \hat{f}_i is the estimated impervious surface fraction of sample i using Sp_SSMA,

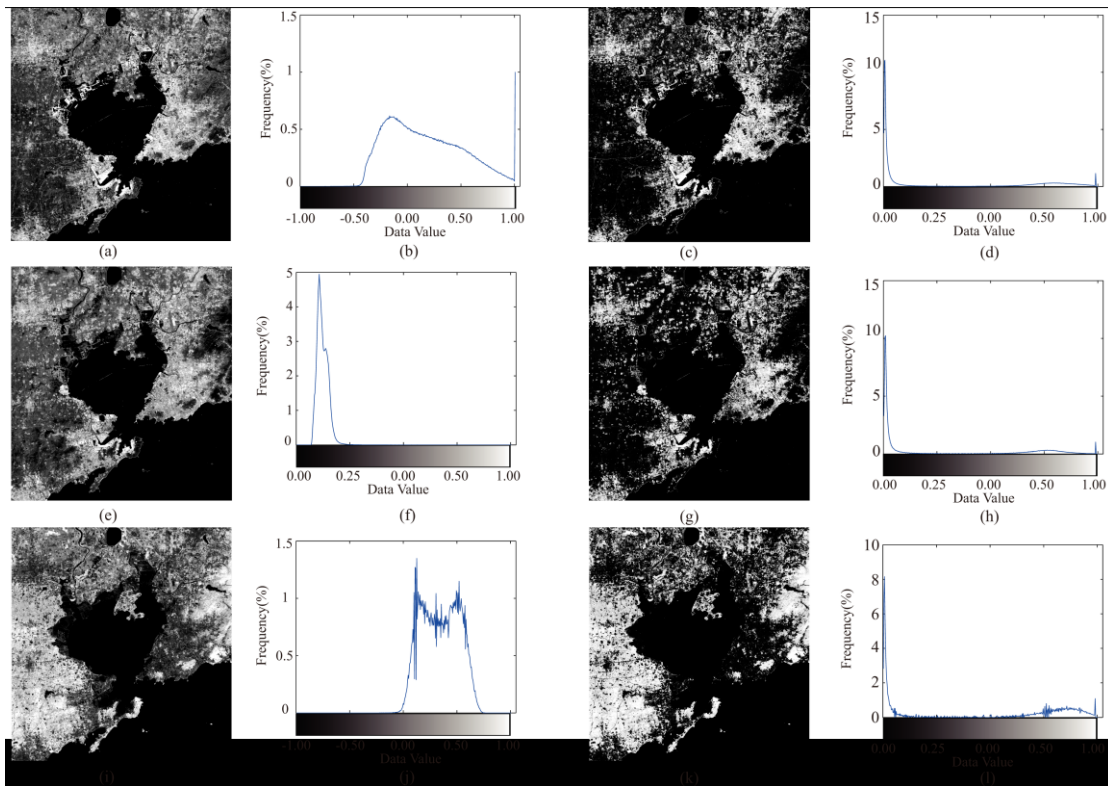
326 $\bar{\hat{f}}$ is the mean value of the samples; f_i is the true impervious surface proportion
327 derived from Google Earth of pixel i ; and N is the number of samples.

328 In order to compare the performance of impervious surface estimation of
329 Sp_SSMA, comparative analysis is performed with a simple fixed four-endmembers
330 SMA (fixed SMA) and the state-of-the-art hierarchical SMA, Prior-knowledge-based
331 spectral mixture analysis (PKSMA) (Zhang et al, 2014). As for fixed SMA and
332 PKSMA, high albedo, low albedo, soil and vegetation are chosen as a fixed set of
333 endmembers. The extreme pixel clusters at MNF-based feature space are utilized to
334 identify the spectral of each endmember.

335

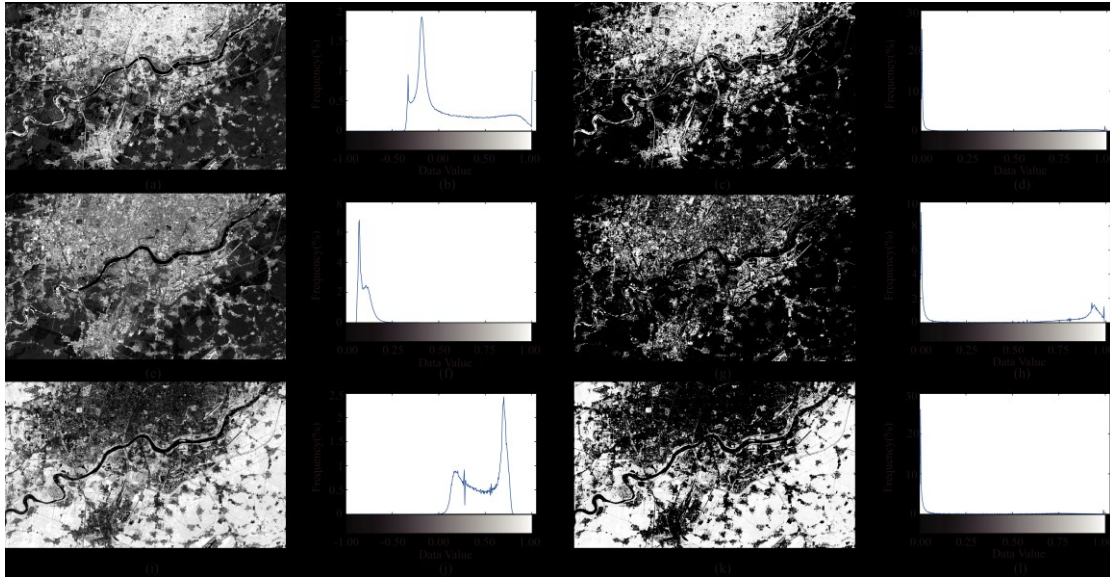
336 4.2 Stratification result

337 As presented in Section 3, the enhanced CBI, I component and NDVI values
 338 were taken to construct the subgroups for spectral unmixing. In this study,
 339 $\lambda_{CBI}, \lambda_I, \lambda_{NDVI}$ are 20 and $\theta_{CBI}, \theta_I, \theta_{NDVI}$ are 0.5 for the normalized indices in both the
 340 images. Figures 4 and 5 show the original indices images and their histograms,
 341 together with the corresponding transformed result the two study areas respectively. It
 342 is clear that the separation between impervious surface and background information in
 343 CBI, I and vegetation and background fraction in NDVI is improved effectively. The
 344 histograms clearly show the apparent separations between the lower and higher values.
 345 It is suggested that the transformation plays an active role in urban image description,
 346 which may have a positive impact on stratification.



347
 348 Figure 4 The transformation for feature indices enhancement in Landsat TM: (a), (e), (i) are the original CBI, I and
 349 NDVI images, (b), (f), (j) are their corresponding histogram images; (c), (g), (k) are the enhanced CBI, I and NDVI
 350 images, (d), (h), (l) are their corresponding histogram images.

351
 352



353
 354 Figure 5 The transformation for feature indices enhancement in ASTER: (a), (e), (i) are the original CBI, I and
 355 NDVI images, (b), (f), (j) are their corresponding histogram images; (c), (g), (k) are the enhanced CBI, I and NDVI
 356 images, (d), (h), (l) are their corresponding histogram images.

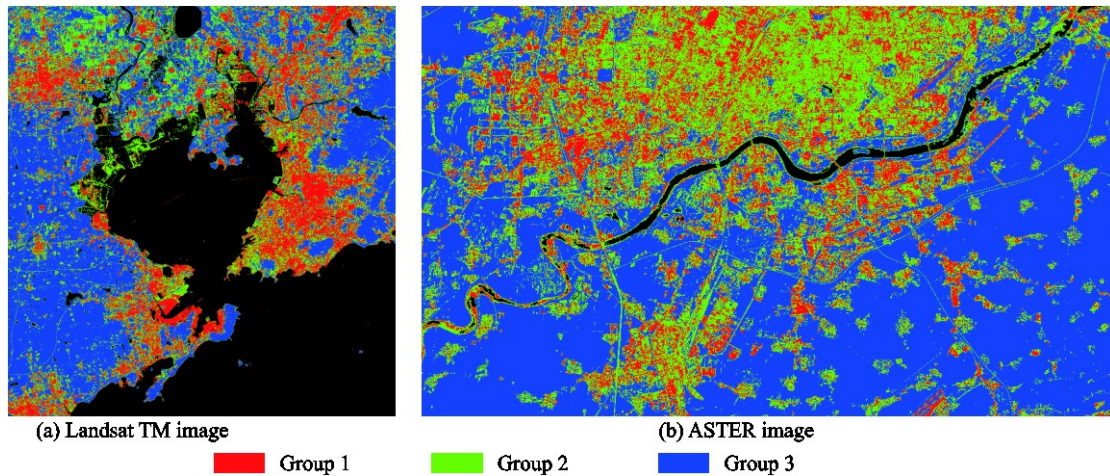
357

358 Table 1. The threshold values.

	Landsat TM	ASTER
CBI_{enh}	0.40	0.42
I_{enh}	0.38	0.38
$NDVI_{enh}$	0.42	0.45

359

360 The automatically selected thresholds and rules for stratification in this
 361 experiment were shown in Table 1. The location of each sub-region obtained by the
 362 stratification rules (Figure 6) illustrates that Group 1 mainly lies in the new distinct in
 363 urban area, while Group 2 mainly lies in the urban fringe, industrial district and
 364 historic town, and Group 3 in suburban area. Further analysis demonstrated that the
 365 three main land cover types show significant differences among three groups. As for
 366 impervious surface, in the area of Group 1, the high and low albedo both present a
 367 relatively higher reflectance comparing with impervious surface fractions in other
 368 subsets. As for Group 2, the impervious surfaces are mainly made up of tile-roofed
 369 historic buildings, industrial area and mixed types of impervious material. The low
 370 albedo impervious surface pixels belong to Group 3 are mainly composed of metal
 371 sheet masonry. When considering the soil fraction, it tends to be composed of nature
 372 impervious land covers, such as sand and stone in construction sites and bare rocks in
 373 Group 1 and artificial land feature such as farmland and wasteland in Group 2. The
 374 nature dark bare soil is predominant in soil fractions in Group 3. Vegetation only
 375 appears in Group 2 and 3. Crops in growing season, nature grasslands, shrub lands
 376 and forest are the main composition in Group 3, whilst some artificial green land in
 377 urban area and urban fringe are graded into Group 2. As results, the three unmixing
 378 models are suitable to be applied to the three groups respectively.



380

381 Figure 6 The stratification result: (a)Landsat TM image, (b)ASTER image.

382

383 In order to evaluate the accuracy of stratification, that is to say, there should be
 384 no vegetation fractions in Group 1 and no high albedo fractions in Group 3, 200 pixels
 385 were randomly selected in Group 1 and 3 in both study sites respectively. The overall
 386 accuracy of the stratification method were 92.75% in Group 1 and 95.50% in Group 3
 387 with the help of Google Earth images as the reference data. The mis-stratifications
 388 were part of the error sources. Therefore, the high accuracy obtained indicates that
 389 this error can be neglected.

390 4.3 Impervious surface abundance

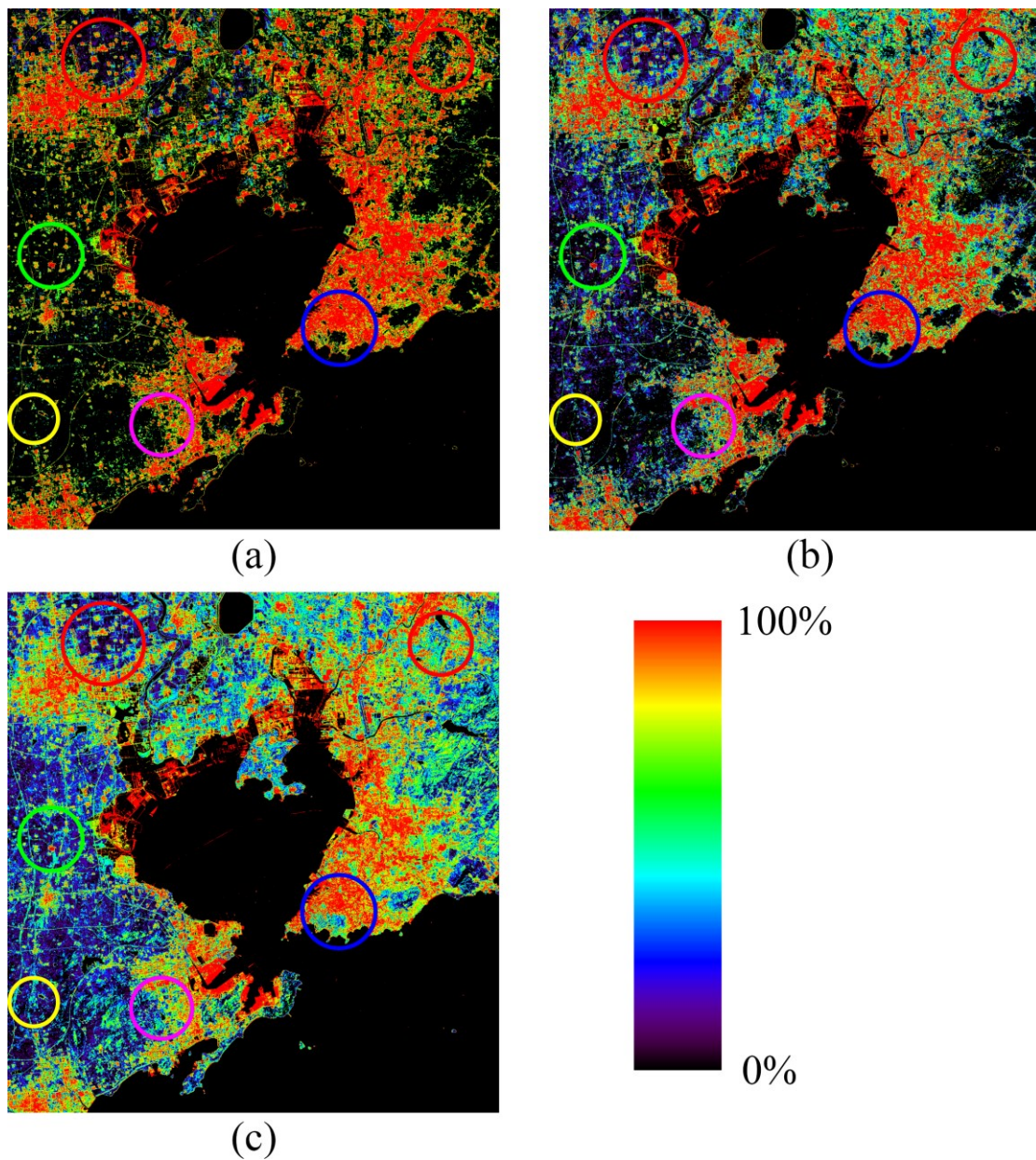
391 With the identified three urban area subgroups and different endmember sets
 392 achieved independently in each subarea, spectral unmixing was performed. The
 393 impervious surface abundance images are reported in [Figures 7\(a\) and 8\(a\)](#). Visual
 394 inspection found that the spatial distribution of impervious surface fraction matches
 395 well with known impervious surface distribution of Qingdao and Shenyang. A
 396 detailed insight into the general pattern of impervious surface fraction saw that the
 397 abundance value was higher in the central business district (CBD) areas and along the
 398 transportation lines, lower in suburban areas, and near zero in the rural and vegetated
 399 areas as expected. However, in less developed areas, especially the areas of Group 3,
 400 several paths of impervious surface areas failed to be recognized which could be a
 401 primary error source.

402 Quantitative validations were also conducted. 400 sites were randomly selected
 403 on the Landsat and ASTER images, respectively, for validation. Each site is a window
 404 of 3 pixels by 3 pixels, covering 90 m by 90 m, since their spatial resolution is 30 m.
 405 180 pixels by 180 pixels on the Google Earth images are associated with each site,
 406 since its spatial resolution is 0.5 m. [The estimated total impervious surface abundance](#)
 407 [for each site is compared with the ground reference provided](#) by the Google Earth

408 images. The reason to utilize a window area to validate the performance is to reduce
409 the problem caused by image registration error.

410 Quantitative analysis in Table 2 indicates that strong positive correlations with
411 reference impervious surface fraction with relatively small RMSE and SE values with
412 an R of 0.89 and 0.83, SE of 2.37% and 3.59%, whilst RMSE of 10.24% and 12.57%
413 respectively. With a detailed analysis, we see a better performance is achieved in
414 developed areas (e.g. an R of 0.86 and 0.81, an SE of 0.91% and 1.58%, a RMSE of
415 8.53% and 11.91%) when compared to less developed areas (e.g. an R of 0.84 and
416 0.79, an SE of 5.23% and 4.86%, RMSE of 12.89% and 15.32%).

417



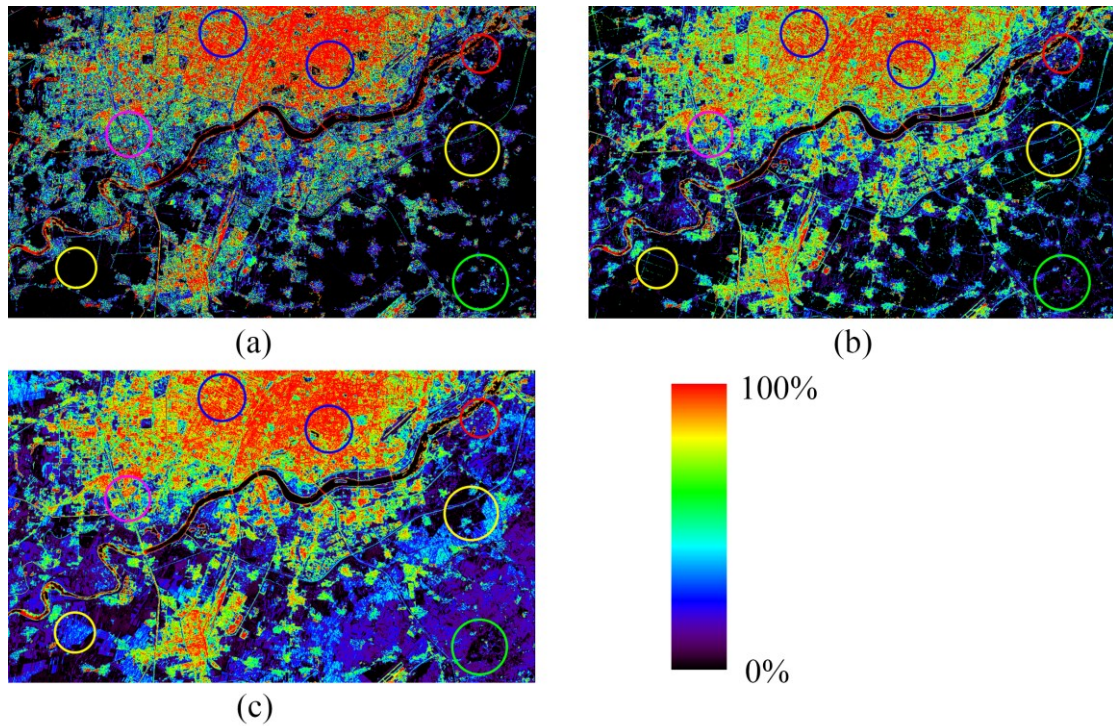
418

419 Figure 7 The impervious surface abundance images of Landsat TM using Sp_SSMA (a), PKSMA (b) and

420 fixed-SMA(c).

421

422



423

424

Figure 8 The impervious surface abundance images of ASTER using Sp_SSMA (a), PKSMA (b) and fixed-SMA(c).

425

426

427

Table 2. Accuracy assessment of impervious surfaces with Sp_SSMA, PKSMA and fixed- SMA.

		Sp_SSMA		PKSMA		Fixed-SMA	
		Landsat	ASTER	Landsat	ASTER	Landsat	ASTER
Over all	R	0.89	0.83	0.84	0.76	0.79	0.75
	RMSE	10.24%	12.57%	11.24%	17.10%	15.13%	19.28%
	SE	2.37%	3.59%	3.47%	6.11%	5.09%	8.19%
Developed	R	0.86	0.81	0.89	0.63	0.73	0.63
	RMSE	8.53%	11.91%	9.72%	14.91%	15.52%	13.02%
	SE	0.91%	1.58%	1.43%	-3.91%	-8.18%	3.34%
Less-developed	R	0.84	0.79	0.76	0.64	0.81	0.51
	RMSE	12.89%	15.32%	14.76%	19.49%	14.13%	21.22%
	SE	5.23%	4.86%	8.05%	8.47%	7.84%	12.47%

428

429

430 *4.4 Comparative analysis*

431 To demonstrate the effectiveness of proposed Sp_SSMA, PKSMA (Figures 7(b)
432 and 8(b)) and fixed-SMA (Figures 7(c) and 8(c)) were carried out for comparison.
433 Through a visual qualitative comparison, a similar impervious surface distribution
434 illustration is observed in most parts of the study sites. Impervious surface of high
435 abundance lies along the coastline and the northwest portion with low fraction in
436 suburban and rural areas in Qingdao. The ASTER image, which covers an urban
437 transect in the region of Shenyang, possesses a higher impervious surface fraction
438 values in the north part of the study area.

439 However, severe misestimation can be observed in both four-endmember SMA
440 and PKSMA. Generally, an overestimation can be observed in suburban and rural
441 areas while the impervious surface abundance value of inner-city regions is more
442 likely to be under-estimated in fix-SMA and PKSMA. The area in magenta circle is
443 impervious surface mixed up with pervious materials. An obvious overestimation is
444 observed in PKSMA in Figures 7(b) and 8(b). The land surface in red circles on
445 Figures 7 and 8, which are graded in Group 2 in Sp_SSMA, are ought to be mainly
446 composed of farmland and other pervious surface which have extremely low
447 impervious surface fraction values. Severe over-estimation can be observed in both
448 PKSMA and four-endmember SMA. As for the area with high impervious surface
449 fraction values, PKSMA and four-endmember SMA tend to be underestimated. On
450 one hand, the small impervious surface patches in green circles in suburban and rural
451 areas which are supposed to have high impervious surface abundance, are
452 undervalued seriously in four-endmember SMA and PKSMA. On the other hand,
453 PKSMA and fixed-SMA tend to underestimate the impervious surface fraction values
454 in the highly urbanized old districts as marked by blue circles. This phenomenon is
455 much more obvious in Shenyang city as reported in Figure 8. The reason lies in the
456 inability of entire-image-achieved endmember spectrum in expressing the complex
457 impervious surface constitution, especially in the historic towns. Shenyang, in
458 particular, is composited of diverse industrial, commercial and residential landscape
459 that can be traced from decades ago to present day. The industrial and economic
460 development transformation also contributed to the complexity of impervious surface
461 types. The results indicate that it is important that the endmembers subsets are
462 extracted and applied in each group of data separately and highlight the advantage of
463 spectral domain stratification. However, Sp_SSMA shows a relative poor performance
464 in mapping transportation lines when compared with four-endmember SMA and
465 PKSMA as shown by the region in yellow circle. The reason lies in that transportation
466 lines are likely to be mixed up with pervious surface in suburban or rural areas due to
467 the limited resolution. The absence of the representative endmembers leads to the
468 poor performance on transportation lines.

469 The quantitative results of accuracy assessment via R, RMSE and SE are
470 reported in Table 2. Note that these accuracy assessments were calculated for the
471 entire image, and for developed areas (impervious surface abundance great than or
472 equal to 30%) and less-developed areas (impervious surface abundance less than 30%)

473 as well. The quantitative accuracy assessment in Table 2 shows that the overall
474 performance of the Sp_SSMA is better than the others, with R of 0.79 and 0.75, SE of
475 5.09 % and 8.19%, RMSE of 15.13% and 19.28% for simple four-endmember SMA,
476 while R of 0.84 and 0.76, SE of 3.47 % and 6.11%, RMSE of 11.24% and 17.10% for
477 PKSMA. As for the fixed-endmember SMA, a much higher error level was observed.
478 Further analyses reveal that a severe over-estimation is given by PKSMA and
479 four-endmember SMA in less developed areas with significantly high values of SE,
480 and RMSE. That's because in PKSMA, some low-density areas were misclassified as
481 high-density areas, resulting some soil were regarded as impervious surface during
482 spectral unmixing processes on one hand. Moreover, in order to ensure the integrity of
483 impervious surface information, NDVI and RED band doesn't always perform well in
484 eliminate vegetation information. On the other hand, the endmember sets for all
485 subsets in PKSMA were chosen through the original image while different
486 combinations were applied for each subgroup. It ignored the variability within each
487 land feature class which would lead to confusion between land cover with similar
488 spectral characteristics. For developed areas, the performance of the PKSMA and the
489 proposed SMA method is satisfactory and comparable in new-districts-dominated
490 Qingdao, with old-districts-dominated Shenyang on the opposite site. When compared
491 to Sp_SSMA, PKSMA undervalued some high abundance impervious surface in rural
492 area with low density due to the confusion with soil. As for regions with high
493 impervious surface fraction in urban area, overestimation can be observed due to the
494 absence of soil endmember in high-density new district areas in PKSMA whilst old
495 districts are suffering from underestimation. Meanwhile, PKSMA achieved a slightly
496 better performance than that of Sp_SSMA in transportation lines.

497

498 5 Conclusions

499 In this paper, a stratified spectral mixture analysis in spectral domain (Sp_SSMA)
500 method was presented for estimating the impervious surface fraction in urban areas
501 through stratification. The Sp_SSMA takes advantage of the features of CBI, I
502 component and NDVI to stratify the entire image into three subareas, named Group 1,
503 Group 2 and Group 3. The performance of Sp_SSMA is demonstrated through the
504 relationship with the impervious surfaces abundance derived from Sp_SSMA and
505 manual digitizing which are regarded as ground reference. Moreover, visual
506 inspection and quantitative analysis show that Sp_SSMA improved the accuracy of
507 impervious surface estimation when compared with the existing LSMA-based method
508 (e.g. fixed-SMA, PKSMA). A further analysis suggests that Sp_SSMA estimates
509 impervious surface abundances in both developed and less-developed areas with
510 satisfying results. The proposition of Sp_SSMA improved the accuracy of mapping
511 impervious surface fraction with simple and convenient image stratification approach
512 which may offer a help to urban land use management.

513 It can be considered that implementing the stratification approach into

514 impervious surface abundance estimation may further reduce the spectral similarity
515 between impervious surface and bare soil and reduce the within class variability in
516 each subgroup. Though the three land cover types still suffer from intra-class
517 variability due to the complex light scattering mechanisms in surface objects, different
518 constituent materials, the differences between impervious surfaces are small enough
519 to be represented by 1 or 2 endmembers while vegetation and soil can be
520 characterized by 1 endmember respectively. Thus, Sp_SSMA can promise more
521 reliable impervious surface fraction estimation. However, there are still confusions
522 between impervious surface and soil in urban fringe, since the land use structures are
523 tend to be disordered and the spectral information of impervious surface and bare soil
524 is quite alike.

525 Another advantage of the proposed Sp_SSMA is that it takes advantage of
526 stratification information to select endmembers in each sub-group independently.
527 While stratification has been studied extensively [32], [38]-[40], little research has
528 been conducted to consider the spectral variability in different subareas. Although the
529 existing researches applied different endmembers to different subset, the endmembers
530 were achieved from the entire image scene rather than each sub-area that have been
531 classified. The Sp_SSMA takes advantage of the reduction of spectral confusion
532 between similar objects and within class variability in each sub-group to obtain
533 endmembers in each sub-group independently. Therefore, by using Sp_SSMA, inner
534 layer information is made the best use.

535 Even though Sp_SSMA markedly improved the accuracy of impervious surface
536 estimation, confusion between impervious surface and soil in suburban areas is still a
537 major concern. This confusion results in the overestimation of impervious surface
538 abundance in suburban and rural areas. More effort is still needed to address this
539 dilemma. In addition, less estimation of the traffic roads in the rural areas is another
540 problem to overcome. Furthermore, the accuracy and efficiency of stratification
541 affects the result of impervious surface abundance extraction largely. Specifically, the
542 non-existing of a specific land cover endmember, such as transformation lines in
543 Group 2, may lead to misestimation of impervious surface fraction. Future research is
544 needed to enhance the stratification model with more divisibility between land cover
545 features with similar characteristics.

546 **Acknowledgements**

547 This work was supported by Chinese Natural Science Foundation Projects
548 (41471353) and National Key Research and Development Program of China (Project
549 Ref. No. 2016YFB0501501).
550

551 **Reference:**

- 552 Burazerovic, D., Heylen, R., Geens, B., Sterckx, S., & Scheunders, P., 2013.
553 Detecting the adjacency effect in hyperspectral imagery with spectral unmixing
554 techniques. *IEEE Journal of Selected Topics in Applied Earth Observations & Remote*
555 *Sensing*, 6(3), 1070-1078.
- 556 Conway, T. M., 2007. Impervious surface as an indicator of ph and specific
557 conductance in the urbanizing coastal zone of New Jersey, USA. *Journal of*
558 *Environmental Management*, 85(2), 308-16.
- 559 Córdoba-Matson, M. V. Gutiérrez, J. and Porta-Gándara, M. Á., 2010. Evaluation
560 of *Isochrysis galbana* (clone T-ISO) cell numbers by digital image analysis of color
561 intensity. *Journal of applied phycology*, 22(4), 427-434.
- 562 Coseo, P., & Larsen, L., 2014. How factors of land use/land cover, building
563 configuration, and adjacent heat sources and sinks explain urban heat islands in
564 Chicago. *Landscape & Urban Planning*, 125(6), 117-129.
- 565 Deng, C., & Wu, C., 2013. A spatially adaptive spectral mixture analysis for mapping
566 subpixel urban impervious surface distribution. *Remote Sensing of Environment*,
567 133(12), 62-70.
- 568 Deng, C., & Wu, C., 2013. The use of single-date modis imagery for estimating
569 large-scale urban impervious surface fraction with spectral mixture analysis and
570 machine learning techniques. *Isprs Journal of Photogrammetry & Remote Sensing*,
571 86(4), 100-110.
- 572 Du, Q., & Du, P., 2014. Modified multiple endmember spectral mixture analysis for
573 mapping impervious surfaces in urban environments. *Journal of Applied Remote*
574 *Sensing*, 8(1), 5946-5957.
- 575 Du, S., Shi, P., Rompaey, A. V., & Wen, J., 2015. Quantifying the impact of
576 impervious surface location on flood peak discharge in urban areas. *Natural Hazards*,
577 76(3), 1457-1471.
- 578 Foody, G. M., Lucas, R. M., Curran, P. J., & Honzak, M., 1997. Non-linear mixture
579 modelling without end-members using an artificial neural network. *International*
580 *Journal of Remote Sensing*, 18(18), 937-953.
- 581 Gao, B. C., 1996. NDWI—a normalized difference water index for remote sensing of
582 vegetation liquid water from space. *Proc Spie*, 58(3), 257-266.
- 583 Hu, T., Yang, J., Li, X., & Gong, P., 2016. Mapping urban land use by using Landsat
584 images and open social data. *Remote Sensing*, 8(2), 151.
- 585 Hu, X. & Weng Q., 2008. Estimating impervious surfaces from medium spatial
586 resolution imagery: a comparison between fuzzy classification and LSMA.
587 *Catastrophe and contention in rural China* :. Cambridge University Press.
- 588 Hu, X., & Weng, Q., 2009. Estimating impervious surfaces from medium spatial
589 resolution imagery using the self-organizing map and multi-layer perceptron neural
590 networks. *Remote Sensing of Environment*, 113(10), 2089-2102.
- 591 Huang, C. & Townshend. J. R. G., 2003. A stepwise regression tree for nonlinear
592 approximation: applications to estimating subpixel land cover. *International Journal of*
593 *Remote Sensing*, 24(1), 75-90.

594 Huete, A. R., 1988. A soil-adjusted vegetation index (SAVI). *Remote Sensing of*
595 *Environment*, 25(3), 295-309.

596 Kaspersen, P., Fensholt, R., & Drews, M., 2015. Using Landsat vegetation indices to
597 estimate impervious surface fractions for European cities. *Remote Sensing*, 7,
598 8224-8249.

599 Kato, S., & Yamaguchi, Y., 2007. Estimation of storage heat flux in an urban area
600 using aster data. *Remote Sensing of Environment*, 110(1), 1-17.

601 Kotarba, A. Z, Aleksandrowicz, S., 2016. Impervious surface detection with nighttime
602 photography from the International Space Station. *Remote Sensing of Environment*,
603 176, 295-307.

604 Liu, J., Fang, T., & Li, D., 2011. Shadow detection in remotely sensed images based
605 on self-adaptive feature selection. *IEEE Transactions on Geoscience & Remote*
606 *Sensing*, 49(12), 5092-5103.

607 Liu, T., & Yang, X., 2013. Mapping vegetation in an urban area with stratified
608 classification and multiple endmember spectral mixture analysis. *Remote Sensing of*
609 *Environment*, 133(12), 251-264.

610 Lu, D., & Weng, Q., 2004. Spectral mixture analysis of the urban landscape in
611 indianapolis with landsat ETM+ imagery. *Photogrammetric Engineering & Remote*
612 *Sensing*, 70(9), 1053-1062.

613 Lu, D., & Weng, Q., 2006. Use of impervious surface in urban land-use classification.
614 *Remote Sensing of Environment*, 102(1-2), 146-160.

615 Lu, D., & Weng, Q., 2009. Extraction of urban impervious surfaces from an Ikonos
616 image. *International Journal of Remote Sensing*, 30(5), 1297-1311.

617 Mohapatra, R. P. & Wu, C., 2008. Subpixel imperviousness estimation with IKONOS
618 imagery: an artificial neural network approach, Taylor & Francis Group: London, UK,
619 21-37.

620 Otsu, N., 1979. A threshold selection method from gray-level histograms. *IEEE*
621 *Transactions on Systems Man & Cybernetics*, 9(1), 62-66.

622 Powell, R. L., Roberts, D. A., Dennison, P. E., & Hess, L. L., 2007. Sub-pixel
623 mapping of urban land cover using multiple endmember spectral mixture analysis:
624 manaus, brazil. *Remote Sensing of Environment*, 106(2), 253-267.

625 Rashed, T., Weeks, J. R., Roberts, D., Rogan, J., & Powell, R., 2003. Measuring the
626 physical composition of urban morphology using multiple endmember spectral
627 mixture models. *Photogrammetric Engineering & Remote Sensing*, 69(9), 1011-1020.

628 Roessner, S., Segl, K., Heiden, U., & Kaufmann, H., 2001. Automated differentiation
629 of urban surfaces based on airborne hyperspectral imagery. *IEEE Transactions on*
630 *Geoscience & Remote Sensing*, 39(7), 1525-1532.

631 Rouse, J. W. Haas R. H., Deering, D. W. Schell, J. A. and Harlan, J. C., 1974.
632 Monitoring the vernal advancement and retrogradation (green wave effect) of natural
633 vegetation. NASA/GSFC Type III Final Report, Greenbelt, MD., 371.

634 Sexton, J. O., Song, X. P., Huang, C., Channan, S., Baker, M. E., & Townshend, J. R.,
635 2013. Urban growth of the Washington, D.C.–baltimore, md metropolitan region from
636 1984 to 2010 by annual, Landsat-based estimates of impervious cover. *Remote*
637 *Sensing of Environment*, 129(2), 42-53.

638 Small, C., & Milesi, C., 2013. Multi-scale standardized spectral mixture models.
639 Remote Sensing of Environment, 136(5), 442-454.

640 Small, C., 2001. Estimation of urban vegetation abundance by spectral mixture
641 analysis. International Journal of Remote Sensing, 22(22), 299-307.

642 Somers, B., Delalieux, S., Verstraeten, W. W., & Verbesselt, J., 2009. Magnitude- and
643 shape-related feature integration in hyperspectral mixture analysis to monitor weeds
644 in citrus orchards. Geoscience & Remote Sensing IEEE Transactions on, 47(11),
645 3630-3642.

646 Sun, G., Chen, X., Jia, X., & Yao, Y., 2015. Combinational build-up index (cbi) for
647 effective impervious surface mapping in urban areas. IEEE Journal of Selected Topics
648 in Applied Earth Observations & Remote Sensing, 9(5), 1-12.

649 Wang, Z., Gang, C., Li, X., Chen, Y., & Li, J., 2015. Application of a normalized
650 difference impervious index NDII to extract urban impervious surface features based
651 on Landsat TM images. International Journal of Remote Sensing, 36(4), 1055-1069.

652 Weng, Q. H., Hu, X. F., & Liu, H., 2009. Estimating impervious surfaces using linear
653 spectral mixture analysis with multitemporal aster images. International Journal of
654 Remote Sensing, 30(18), 4807-4830.

655 Weng, Q., 2012. Remote sensing of impervious surfaces in the urban areas:
656 requirements, methods, and trends. Remote Sensing of Environment, 117(2), 34-49.

657 Weng, Q., Hu, X. & Lu, D., 2008. Extracting impervious surfaces from medium
658 spatial resolution multispectral and hyperspectral imagery: a comparison.
659 International Journal of Remote Sensing, 29(11), 3209-3232.

660 White, M. D., & Greer, K. A., 2006. The effects of watershed urbanization on the
661 stream hydrology and riparian vegetation of los penasquitos creek, california.
662 Landscape & Urban Planning, 74(2), 125-138.

663 Wu, C., & Murray, A. T., 2003. Estimating impervious surface distribution by spectral
664 mixture analysis. Remote Sensing of Environment, 84(4), 493-505.

665 Wu, C., & Murray, A. T., 2005. A cokriging method for estimating population density
666 in urban areas. Computers Environment & Urban Systems, 29(5), 558-579.

667 Wu, C., 2004. Normalized spectral mixture analysis for monitoring urban composition
668 using ETM+ imagery. Remote Sensing of Environment, 93(4), 480-492.

669 Xian, G., Crane, M., & Su, J., 2007. An analysis of urban development and its
670 environmental impact on the Tampa bay watershed. Journal of Environmental
671 Management, 85(85), 965-76.

672 Yang, F., Matsushita, B., & Fukushima, T., 2010. A pre-screened and normalized
673 multiple endmember spectral mixture analysis for mapping impervious surface area in
674 lake Kasumigaura basin, Japan. Isprs Journal of Photogrammetry & Remote Sensing,
675 65(5), 479-490.

676 Yang, J., & He, Y., 2017. Automated mapping of impervious surfaces in urban and
677 suburban areas: linear spectral unmixing of high spatial resolution imagery.
678 International Journal of Applied Earth Observation & Geoinformation, 54, 53-64.

679 Yang, L., Huang, C., Homer, C. G., Wylie, B. K., & Coan, M. J., 2003. An approach
680 for mapping large-area impervious surfaces: synergistic use of landsat-7 ETM+ and
681 high spatial resolution imagery. Canadian Journal of Remote Sensing, 29(2), 230-240.

682 Yang, S., & Lunetta, R. S., 2011. Sub-pixel mapping of tree canopy, impervious
683 surfaces, and cropland in the Laurentian Great Lakes basin using MODIS time-series
684 data. *IEEE Journal of Selected Topics in Applied Earth Observations & Remote*
685 *Sensing*, 4(2), 336-347.

686 Yang, X., & Liu, Z., 2005. Use of satellite-derived landscape imperviousness index to
687 characterize urban spatial growth. *Computers Environment & Urban Systems*, 29(5),
688 524-540.

689 Yuan, F., & Bauer, M. E., 2007. Comparison of impervious surface area and
690 normalized difference vegetation index as indicators of surface urban heat island
691 effects in Landsat imagery. *Remote Sensing of Environment*, 106(3), 375-386.

692 Zhang, H., Lin, H., Li, Y., Zhang, Y., & Fang, C., 2016. Mapping urban impervious
693 surface with dual-polarimetric SAR data: an improved method. *Landscape & Urban*
694 *Planning*, 151, 55-63.

695 Zhang, J., He, C., Zhou, Y., Zhu, S., & Shuai, G., 2014. Prior-knowledge-based
696 spectral mixture analysis for impervious surface mapping. *International Journal of*
697 *Applied Earth Observation & Geoinformation*, 28(5), 201-210.

698 Zhang, L. X., Wang, J., Wang, X., & Zhao, J. P., 2007. Competency model of top
699 managers of state-owned enterprise in China's northeastern old industrial base. *Journal*
700 *of Northeastern University*, 28(4), 600-604.

701 Zhang, Y., Zhang, H., & Lin, H., 2014. Improving the impervious surface estimation
702 with combined use of optical and SAR remote sensing images. *Remote Sensing of*
703 *Environment*, 141(2), 155-167.

704 Zhou, Y., & Wang, Y. Q., 2008. Extraction of impervious surface areas from high
705 spatial resolution imagery by multiple agent segmentation and classification.
706 *Photogrammetric Engineering & Remote Sensing*, 74(7), 857-868.

707